

A One-Parameter Family of Time-Symmetric Initial Data for the Radial Infall of a Particle into a Schwarzschild Black Hole

Karl Martel and Eric Poisson

Department of Physics, University of Guelph,

Guelph, Ontario, Canada N1G 2W1

(Dated: November 4, 2018)

Abstract

A one-parameter family of time-symmetric initial data for the radial infall of a particle into a Schwarzschild black hole is constructed within the framework of black-hole perturbation theory. The parameter measures the amount of gravitational radiation present on the initial spacelike surface. These initial data sets are then evolved by integrating the Zerilli-Moncrief wave equation in the presence of the particle. Numerical results for the gravitational waveforms and their power spectra are presented; we show that the choice of initial data strongly influences the waveforms, both in their shapes and their frequency content. We also calculate the total energy radiated by the particle-black-hole system, as a function of the initial separation between the particle and the black hole, and as a function of the choice of initial data. Our results confirm that for large initial separations, a conformally-flat initial three-geometry minimizes the initial gravitational-wave content, so that the total energy radiated is also minimized. For small initial separations, however, we show that the conformally-flat solution no longer minimizes the energy radiated.

PACS numbers: 04.70.Bw, 04.30.Db, 04.30.Nk

I. INTRODUCTION

Due to the advent of laser-interferometric gravitational-wave detectors, there is a strong possibility that gravitational waves from black-hole collisions will be detected in the near future. Black-hole mergers are good candidates for detection because of the strength of the gravitational waves they emit, and of the relatively high expected event rate[1]. Detection of these collisions and successful extraction of the black-hole parameters require a detailed theoretical understanding of the gravitational waves emitted during the collision. The lack of solutions to the dynamical two-body problem in general relativity renewed interest in simulating black-hole collisions by numerically integrating the full non-linear Einstein field equations[2, 3, 4, 5, 6, 7, 8, 9, 10]. The challenge is enormous. For a recent review of the field of numerical relativity, see [11].

From a numerical point of view, long-term simulations of black-hole collisions are limited by the available memory[6] and instabilities associated with the numerical implementation of the full non-linear equations[3, 8, 12]. Because of these difficulties, numerical relativity is not yet at the stage where it can simulate black-hole collisions for a very long time[9]. Most simulations are started at a late stage of the collision, when the two black holes are separated by a distance of just a few black-hole masses. These small initial separations imply that non-trivial initial values must be provided for the gravitational field in order to start the numerical evolution.

The initial-value problem consists of finding an initial three-metric γ_{ij} , and an initial extrinsic curvature K_{ij} , that encode all of the physical information about the system. The solution should contain information about the state of motion of the black holes, and information about the gravitational-wave content of the initial three-surface. The initial gravitational-wave content is important because it contains information about the motion of the black holes prior to the beginning of the numerical evolution. (In the past of the initial hypersurface, the two black holes emitted gravitational waves that must be accounted for in the initial data.) As we will see in Sec. III, the initial gravitational-wave content can play an important role in the modeling of the gravitational waveforms.

For the case of colliding black holes, various methods have been developed to find initial data that satisfy the Hamiltonian and momentum constraints of general relativity, e.g., the apparent-horizon method[13], conformal-imaging method[14], and puncture method[15].

The starting point in these methods is a maximally embedded initial spacelike slice ($K^i_i = 0$). On this slice, the geometry is described by a conformally-flat initial metric, $\gamma_{ij} = \Psi^4 \bar{\gamma}_{ij}$, and a rescaled traceless extrinsic curvature $K_{ij} = \Psi^{-2} \bar{K}_{ij}$, where $\bar{\gamma}_{ij}$ is the metric of three-dimensional flat space, Ψ the conformal factor, and \bar{K}_{ij} the traceless conformal extrinsic curvature. With these choices, the momentum constraints in vacuum can be recast in terms of quantities defined in the flat space: $\bar{\nabla}^j \bar{K}_{ij} = 0$, where $\bar{\nabla}^i$ is the flat-space covariant derivative. Bowen and York obtained solutions to this equation[16] in terms of a vector field \bar{V}^i that contains information about the spins and linear momenta of the holes on the initial surface, i.e. $\bar{K}^{ij} = \bar{\nabla}^i \bar{V}^j + \bar{\nabla}^j \bar{V}^i - 2/3 \bar{\gamma}^{ij} \bar{\nabla}^k \bar{V}_k$; explicit forms for \bar{V}^i can be found in [17]. The three techniques mentioned above rely on the Bowen-York solutions to construct \bar{K}_{ij} , but because of the different choices of topology for the initial hypersurface, the \bar{K}_{ij} 's they obtain are different. But since the differences in initial topology are mostly hidden behind the event horizons of the black holes, they cannot affect significantly the resulting dynamics. To reflect this, we will generically refer to a K_{ij} based on the Bowen-York solutions as a “longitudinal extrinsic curvature”.

Thus, solutions to the initial-value problem can be generated, but the real problem is to construct physically suitable solutions. This is a difficult problem because of the nonlinearities inherent to the theory. It is very hard in practice to identify which components of γ_{ij} and K_{ij} are to be constrained, and which are to be associated with dynamical and gauge degrees of freedom. It is now widely accepted that choosing a conformally-flat γ_{ij} and a longitudinal K_{ij} are unlikely to yield physically relevant initial data sets.

For example, the assumption that the initial metric of a black-hole binary is conformally flat is likely to be inappropriate, because the metric is known not to be conformally flat at the second post-Newtonian order[17]. As well, any physical black hole is likely to be rotating and, in this case, the assumption of conformal flatness yields poor initial data. The reason for this is well known: Garat and Price[18] have shown that there is no spatial slicing of the Kerr solution that is both axisymmetric and conformally flat, and reduces smoothly to the Schwarzschild solution in the no-rotation limit. The techniques mentioned above can nevertheless provide solutions to the initial-value problem that represent a rotating black hole, but the solutions cannot correspond to a stationary Kerr black hole; there must be some gravitational radiation on the initial slice.

Even in the case of a perturbed Schwarzschild black hole, where conformally-flat slices

can be constructed, the solutions obtained with a longitudinal extrinsic curvature are not necessarily adequate. Lousto and Price[19] have shown that for the head-on collision of two nonrotating black holes in which one of the holes is much less massive than the other, conformally-flat γ_{ij} and longitudinal K_{ij} data (CFL data) do not reproduce the numerical results[19]. In their analysis, they imposed the CFL data at a time t_o and evolved it forward in time. They then looked at the conditions at a later time t_1 , and found that the extrinsic curvature extracted from the numerical data matched poorly with the extrinsic curvature obtained at $t = t_1$ from CFL data. Instead, they found that the extrinsic curvature was better represented by postulating a convective time derivative[20], which means essentially that the time derivative of the metric is proportional to the four-velocity of the small black hole.

The various problematic issues associated with the initial-value problem can be better understood by having recourse to approximate methods[21, 22]. For large initial separations and slow-motion processes, post-Newtonian (PN) theory is useful, especially when the PN metric of two point masses is matched, in a buffer region, with the metric of two distorted Schwarzschild black holes[23]. For small mass ratios, black-hole perturbation theory can be very useful[24, 25, 26, 27], since in this case there is no restriction on the velocity of the small body.

This paper is the first of a series in which, following Lousto and Price[19, 20, 28], the initial-value problem will be systematically explored in black-hole perturbation theory. Our goal is to explore the space of solutions to better identify physically realistic situations (within the domain of validity). This, we hope, will help us understand the essential features that should be possessed by a solution to the initial-value problem. In this paper we look at the radial infall of a particle starting from rest at a radius r_o outside a Schwarzschild black hole, and we construct a one-parameter family of solutions to the initial-value problem. The parameter, α , measures the amount of radiation present on the initial hypersurface. For $\alpha = 1$ the initial metric is conformally flat, a choice of initial data that was previously considered by Lousto and Price[28]. Starting from our family of initial data, we calculate the time evolution of the gravitational perturbations produced by the infalling particle. We then calculate the gravitational waveforms, their power spectra, and the total energy radiated. In this way, we are able to explore the limitations of the assumption of conformal flatness, and determine when the contamination of the gravitational waveforms, due to unphysical

radiation on the initial three-surface, becomes important.

The paper is organized as follows. In Sec. II we give a short overview of black-hole perturbation theory, appropriately restricted to the specific case of radial infall into a Schwarzschild black hole. The evolution of the metric perturbations, governed by an inhomogeneous wave equation, is described in Sec. II A. Our one-parameter family of solutions to the initial-value problem is constructed in Sec. II B. Section III is divided into four subsections. In Sec. III A we explain the numerical method used to integrate the wave equation in the presence of the particle. In Sec. III B we present the gravitational waveforms extracted from the simulations; we discuss the influence of the choice of initial data on the waveforms. In Sec. III C we calculate the power spectrum of the waveforms for selected values of α and initial separation r_o . In Sec. III D we compute the total energy radiated in the $l = 2, 3,$ and 4 multipole moments of the gravitational radiation field. In Sec. IV we summarize our findings and offer some conclusions. Finally, the Appendix contains a discussion of the convergence properties of our numerical code.

Throughout the paper we use MTW conventions[29] for the metric signature and curvature tensors. Greek indices run from 0 to 3, and Latin indices run over the t and r Schwarzschild coordinates. Geometrized units are used: $G = c = 1$.

II. PERTURBATION THEORY

A. Zerilli-Moncrief Wave Equation

We consider the radial infall of a particle of mass μ , starting from rest at a radius r_o , into a Schwarzschild black hole. The particle creates a small perturbation in the gravitational field of the black hole and the total metric is expressed as $g_{\mu\nu} = g_{\mu\nu}^{\text{Sch}} + h_{\mu\nu}$, where $g_{\mu\nu}^{\text{Sch}}$ is the Schwarzschild metric and $h_{\mu\nu}$ is the perturbation; this can be decomposed into odd-parity (axial) and even-parity (polar) modes, each carrying spherical-harmonic indices l and m [30]. Because of the azimuthal symmetry of the problem, only the polar perturbations are excited by the infalling particle. Our calculations are performed in the Regge-Wheeler gauge[31] in which the perturbation — for a specific l -pole and with $m = 0$ — is written as

$$h_{\mu\nu}^{l0} dx^\mu dx^\nu = Y^{l0}(\theta) \left[(1 - 2M/r) H_0^{l0}(r, t) dt^2 + 2H_1^{l0}(r, t) dt dr + (1 - 2M/r)^{-1} H_2^{l0}(r, t) dr^2 + r^2 K^{l0}(r, t) d\Omega^2 \right], \quad (2.1)$$

where H_0^{l0} , H_1^{l0} , H_2^{l0} , and K^{l0} are the multipole moments of the metric perturbations. Below we will omit the superscripts “ $l0$ ” where there is no risk of confusion.

Inserting the perturbed metric into the Einstein field equations yields a set of seven coupled equations for the four metric perturbations; three of these come from the Hamiltonian and momentum constraints and the other four are evolution equations. (The three remaining field equations describe the axial perturbations of the Schwarzschild black hole.) The equations are decoupled when written in terms of the gauge-invariant Zerilli-Moncrief function[32]:

$$\psi(r, t) = \frac{r}{\lambda + 1} \left\{ K(r, t) + \frac{f}{\Lambda} \left[H_2(r, t) - r \frac{\partial}{\partial r} K(r, t) \right] \right\}, \quad (2.2)$$

where $\lambda = (l+2)(l-1)/2$, $f = 1 - 2M/r$, and $\Lambda = \lambda + 3M/r$. This normalization for ψ differs from the normalization adopted in [21, 27, 33]. A relation between various normalizations used in the literature can be found in Lousto and Price[28]. Our normalization is chosen to agree with theirs.

The evolution of $\psi(r, t)$ is governed by a single inhomogeneous wave equation,

$$\left[-\frac{\partial^2}{\partial t^2} + \frac{\partial^2}{\partial r^{*2}} - V(r) \right] \psi(r, t) = S(r, t), \quad (2.3)$$

where $r^* = r + 2M \ln(r/2M - 1)$ is the tortoise radius,

$$V(r) = \frac{2f}{r^2 \Lambda^2} \left[\lambda^2 (\Lambda + 1) + \frac{9M^2}{r^2} \left(\Lambda - \frac{2M}{r} \right) \right] \quad (2.4)$$

is the Zerilli-Moncrief potential, and

$$\begin{aligned} S(r, t) = & \frac{2}{l(l+1)\Lambda} \left\{ r^2 f \left[f^2 \frac{\partial}{\partial r} Q^{tt} - \frac{\partial}{\partial r} Q^{rr} \right] \right. \\ & \left. - \frac{f^2}{\Lambda r} \left[\lambda(\lambda-1)r^2 + (4\lambda-9)Mr + 15M^2 \right] Q^{tt} + r(\Lambda-f)Q^{rr} \right\}, \end{aligned} \quad (2.5)$$

is the source term appropriate for radial infall. The Q^{ab} 's ($a, b = t, r$) are constructed from the particle's stress-energy tensor:

$$Q^{ab}(r, t) = 8\pi \int T^{ab}(r, t, \theta, \varphi) Y^*(\theta, \varphi) d\Omega, \quad (2.6)$$

where $T^{\alpha\beta} = \mu \int u^\alpha u^\beta \delta^4(x^\nu - x_p^\nu(\tau)) (-g)^{-1/2} d\tau$, τ is proper time along the particle's world line $x_p^\nu(\tau)$, $u^\nu = [\tilde{E}/f, -(\tilde{E}^2 - f)^{1/2}, 0, 0]$ is the four-velocity of the particle, and \tilde{E} is the conserved energy per unit mass. We assume, without loss of generality, that the motion

proceeds along the negative z direction, so that $\theta = 0$ on the world line. Evaluating the integrals in Eq. (2.6) and substituting the results into Eq. (2.5), we obtain¹

$$S(r, t) = 16\pi \frac{\sqrt{(2l+1)/(4\pi)}}{l(l+1)} \frac{\mu f^3}{\tilde{E} \Lambda} \left\{ \delta'(r - r_p(t)) - \left[\frac{(\lambda+1)r - 3M}{r^2 f} - \frac{6M\tilde{E}^2}{\Lambda r^2 f} \right] \delta(r - r_p(t)) \right\}$$

where $r_p(t)$ describes the radial component of the particle's motion, a “ $'$ ” denotes a derivative with respect to r , and we have used $Y^{l0}(0) = \sqrt{(2l+1)/(4\pi)}$, which is appropriate for motion along the z -axis. For the radial infall of a particle starting from rest, $r_p(t)$ is given implicitly by

$$t = -4M\tilde{E} \left\{ -\frac{1}{2} \frac{r_o}{2M} \sqrt{\frac{r_p}{2M}} \sqrt{1 - \frac{r_p}{r_o}} + \sqrt{\frac{r_o}{2M}} \left(1 + \frac{r_o}{4M}\right) \arcsin \sqrt{\frac{r_p}{r_o}} \right. \\ \left. + \frac{1}{4} \frac{1}{\tilde{E}^2} \ln \left[\frac{1 + \frac{r_p}{2M} - 2\frac{r_p}{r_o} - 2\tilde{E} \sqrt{\frac{r_p}{2M}} \sqrt{1 - \frac{r_p}{r_o}}}{1 + \frac{r_p}{2M} - 2\frac{r_p}{r_o} + 2\tilde{E} \sqrt{\frac{r_p}{2M}} \sqrt{1 - \frac{r_p}{r_o}}} \right] - \frac{\pi}{2} \sqrt{\frac{r_o}{2M}} \left(1 + \frac{r_o}{4M}\right) \right\}, \quad (2.8)$$

where $r_o \equiv r_p(t=0)$ is the initial position of the particle, and $\tilde{E} = \sqrt{1 - 2M/r_o}$. In Sec. III we numerically integrate Eq. (2.3) with the source term of Eq. (2.7). The integration of Eq. (2.3) requires the specification of initial data for the Zerilli-Moncrief function: both $\psi(r, t=0)$ and $\frac{\partial}{\partial t}\psi(r, t=0)$ must be known. We shall examine this issue in the next subsection.

The Zerilli-Moncrief function $\psi(r, t)$ is directly related to the gravitational waves received at infinity², and knowledge of $\psi(r, t)$ allows us to calculate the rate at which gravitational waves carry energy to infinity. For a specific l -pole, the luminosity (the gravitational-wave flux integrated over a two-sphere) is given by

$$\frac{d}{du} E_l = \frac{1}{64\pi} \frac{(l+2)!}{(l-2)!} \left(\frac{\partial}{\partial u} \psi \right)^2, \quad (2.9)$$

where $u = t - r^*$ is retarded time. The total energy radiated is obtained by integration:

$$E_l = \frac{1}{64\pi} \frac{(l+2)!}{(l-2)!} \int_{-\infty}^{\infty} du \left(\frac{\partial}{\partial u} \psi \right)^2. \quad (2.10)$$

¹ The source term given here agrees with the source term given in [19, 28] if we substitute “ $(1 - 2M/r_p(t))\delta'(r - r_p(t)) - 2M/r^2\delta(r - r_p(t))$ ” for “ $(1 - 2M/r)\delta'(r - r_p(t))$ ” in our source term.

² With polarization axes oriented along the θ and φ directions, we have that the “plus” polarization of the gravitational field is given by $h_+ = \frac{1}{2}\sqrt{(l+2)(l+1)l(l-1)}\psi(u) {}_{-2}Y^{l0}(\theta, \varphi)/r$, where ${}_{-2}Y^{l0}$ are spin-weighted spherical harmonics[34]. The “cross” polarization, in this orientation, is zero.

B. Initial Data

The initial-value problem of general relativity is solved once the metric γ_{ij} and the extrinsic curvature K_{ij} are specified on a three-dimensional spacelike hypersurface. These quantities are not freely specifiable, because they must satisfy the Hamiltonian and momentum constraints of general relativity. Because the constraints are non-linear, finding solutions to the initial-value problem is a non-trivial task, and there is no unique way of doing this. Another essential difficulty is to find solutions that represent a physical situation. In the case of black-hole collisions, γ_{ij} and K_{ij} must represent two moving black holes with some initial amount of gravitational waves, as was explained in the Introduction.

Two much-studied solutions to the initial-value problem are the Misner solution[35] (which is generalized by the conformal-imaging method to situations where the initial hypersurface is not a moment of time-symmetry) and the Brill-Lindquist solution[36] (which is generalized by the puncture method). They represent the spatial metric of two black holes momentarily at rest, and about to undergo a head-on collision. Because the initial hypersurface is a moment of time symmetry, $K_{ij} = 0$ and the initial-value problem reduces to finding γ_{ij} (or the conformal factor). These solutions and their generalizations were used as initial data for the study of the head-on collision of two equal-mass black holes in full numerical relativity[4, 7, 26].

For the problem studied in this paper, namely the radial infall of a small mass μ into a Schwarzschild black hole, we will concentrate on Brill-Lindquist (BL) type initial data. (Our initial data sets are not taken to be inversion symmetric with respect to the throat of the black hole.) The Brill-Lindquist solution can be expanded in powers of μ/M to yield an approximate solution to the initial-value problem appropriate for perturbation theory; in this case $H_1 = 0$ and

$$H_2 = K = 2\mu \frac{\sqrt{4\pi/(2l+1)}}{(1+M/2\bar{r}_o)(1+M/2\bar{r})} \frac{\bar{r}_<^l}{\bar{r}_>^{l+1}}, \quad (2.11)$$

where $\bar{r} = r(1 + \sqrt{f})^2/4$ is the isotropic radius, $f = 1 - 2M/r$, and $\bar{r}_<$ ($\bar{r}_>$) is the smaller (greater) of \bar{r} and \bar{r}_o . This solution was first examined by Lousto and Price[28]. Here we wish to construct a more general solution to the initial-value problem in perturbation theory.

Our initial situation is that of a small mass μ momentarily at rest at a radius r_o outside a Schwarzschild black hole; this is a moment of time symmetry, which implies that $K_{ij} = 0$, so

that the momentum constraints are automatically satisfied. To complete the solution to the initial-value problem, we write the Hamiltonian constraint ${}^3R = 8\pi\rho$ (3R is the Ricci scalar on the initial hypersurface, and ρ is the matter density) in terms of the metric perturbations in the Regge-Wheeler gauge (Eq. (2.1)):

$$\begin{aligned} & -r^2 f \frac{d^2}{dr^2} K - (3r - 5M) \frac{d}{dr} K + r f \frac{d}{dr} H_2 + (H_2 - K) \\ & + \frac{l(l+1)}{2} (H_2 + K) = r^2 f Q^{tt} = 8\pi \sqrt{\frac{2l+1}{4\pi}} \mu \tilde{E} \delta(r - r_o). \end{aligned} \quad (2.12)$$

This is a single equation for two unknowns: the metric functions $K(r)$ and $H_2(r)$. One of the functions can be specified freely, and we do this by postulating the linear relationship $H_2 = \alpha K$, where α is a constant. This is motivated by the fact that the relation $H_2 = K$ produces a metric that is conformally flat:

$$\begin{aligned} ds^2|_{t=0} &= \left(1 + K_{l0}(r) Y_{l0}(\theta)\right) \left(f^{-1} dr^2 + r^2 d\Omega^2\right) \\ &= \left(1 + K_{l0}(r) Y_{l0}(\theta)\right) \left(1 + \frac{M}{2\bar{r}}\right)^4 \left(d\bar{r}^2 + \bar{r}^2 d\Omega^2\right). \end{aligned} \quad (2.13)$$

Making the choice $H_2 = K$ turns Eq. (2.12) into a hypergeometric equation for $K(r)$, and as we shall show below, its solution is given by Eq. (2.11) above. The more general relation $H_2 = \alpha K$ also turns Eq. (2.12) into a hypergeometric equation, for which we will be able to find solutions that generalize Eq. (2.11). Our solutions are parameterized by α , and the procedure outlined here produces a one-parameter family of initial-data sets. Setting $\alpha = 1$ reproduces the BL solution of Eq. (2.11).

Postulating the relation $H_2 = \alpha K$ at the initial moment $t = 0$, Eq. (2.12) becomes ($z \equiv r/2M$)

$$z(1-z) \frac{d^2}{dz^2} K + \left(5/2 - \alpha - (3-\alpha)z\right) \frac{d}{dz} K - \left((1-\alpha) - \frac{l(l+1)}{2}(1+\alpha)\right) K = 0, \quad (2.14)$$

on either side of the particle's initial position ($r \neq r_o$). This is the hypergeometric equation. For $r < r_o$ we must choose a solution that is regular at $r = 2M$, but that is allowed to diverge at $r = \infty$. We denote this solution by $K_{<}(r)$. For $r > r_o$ we must choose a solution that is regular at $r = \infty$, but that may diverge at $r = 2M$. This solution is denoted by $K_{>}(r)$. In terms of these, the solution for $K(r)$ takes the form³

$$K(r, 0) = C(r_o) K_{<}(r_{<}) K_{>}(r_{>}), \quad (2.15)$$

³ In principle, we are free to add any multiple of $K_{>}(r)$ to our particular solution. This represents a different choice of initial three-geometry[19], and we do not consider this possibility here.

where $r_<$ ($r_>$) is the smaller (greater) of r and r_o ,

$$\begin{aligned} K_<(r) &= \left(\frac{r}{2M}\right)^{-b} F\left(b, b-c+1; 1-a+b; \frac{2M}{r}\right), \\ K_>(r) &= \left(\frac{r}{2M}\right)^{-a} F\left(a, a-c+1; 1-b+a; \frac{2M}{r}\right), \end{aligned} \quad (2.16)$$

$F(,;,)$ is the hypergeometric function,

$$\begin{aligned} a &= 1 - \frac{\alpha}{2} + \frac{1}{2} \left[\alpha^2 + 2(1+\alpha)l(l+1) \right]^{1/2}, \\ b &= 1 - \frac{\alpha}{2} - \frac{1}{2} \left[\alpha^2 + 2(1+\alpha)l(l+1) \right]^{1/2}, \\ c &= \frac{5}{2} - \alpha, \end{aligned} \quad (2.17)$$

and $C(r_o)$ is a constant ensuring that $\frac{\partial}{\partial r}K$ has the correct discontinuity at $r = r_o$. Integrating across the δ -function in Eq. (2.12), using $H_2 = \alpha K$ and Eq. (2.15) for K , $C(r_o)$ is easily found to be

$$\begin{aligned} C(r_o) &= 8\pi \frac{\mu}{\tilde{E}} \sqrt{\frac{2l+1}{4\pi}} \frac{1}{r_o^2} \left[K_<(r_o)K'_>(r_o) - K'_<(r_o)K_>(r_o) \right]^{-1} \\ &= 4\pi \sqrt{\frac{2l+1}{4\pi}} \frac{\mu}{M} \left(\frac{r_o}{2M}\right)^{1-\alpha} \frac{\Gamma(r_o)}{\tilde{E}}, \end{aligned} \quad (2.18)$$

where

$$\begin{aligned} \Gamma(r_o) &= \left[aF(a+1, a-c+1; 1-b+a; 2M/r_o)F(b, b-c+1; 1-a+b; 2M/r_o) \right. \\ &\quad \left. - bF(a, a-c+1; 1-b+a; 2M/r_o)F(b+1, b-c+1; 1-a+b; 2M/r_o) \right]^{-1} \end{aligned} \quad (2.19)$$

The second equality in Eq. (2.18) follows from Eq. (15.2.2) of [37] together with Eq. (2.16) to evaluate $K'_<(r_o)$ and $K'_>(r_o)$.

The initial value of the Zerilli-Moncrief function can now be obtained by inserting $K(r)$ and $H_2 = \alpha K(r)$ in Eq. (2.2). This, together with $\frac{\partial}{\partial t}\psi(r, 0) = 0$, completely specifies our family of initial-data sets for the radial infall of a particle starting from rest. In Sec. III we numerically integrate the Zerilli-Moncrief equation for this family of initial data.

The conformally-flat solution can easily be recovered as a special case of the initial-data sets presented above. For a conformally-flat initial three-geometry ($\alpha = 1$), the parameters appearing in the hypergeometric functions (Eq. (2.17)) take the values $a = l + 1$, $b = -l$,

and $c = \frac{3}{2}$, and Eq. (2.16) becomes

$$\begin{aligned}
K_{<}(r) &= \left(\frac{r}{2M}\right)^l F(-l, -l - 1/2; -2l; 2M/r) \\
&= 2^{-(2l+1)} \left(\frac{r}{2M}\right)^l \left(1 + \sqrt{f}\right)^{2l+1} \\
&= \left(\frac{\bar{r}}{2M}\right)^l \frac{1}{1 + M/2\bar{r}}, \tag{2.20}
\end{aligned}$$

$$\begin{aligned}
K_{>}(r) &= \left(\frac{r}{2M}\right)^{-(l+1)} F(l+1, l+1/2; 2(l+1); 2M/r) \\
&= 2^{2l+1} \left(\frac{r}{2M}\right)^{-(l+1)} \left(1 + \sqrt{f}\right)^{-(2l+1)} \\
&= \left(\frac{2M}{\bar{r}}\right)^{l+1} \frac{1}{1 + M/2\bar{r}}, \tag{2.21}
\end{aligned}$$

where we have used Eq. (15.1.13) of [37]. With these results, it is a trivial matter to show that

$$K_{<}(r_{<})K_{>}(r_{>}) = \frac{2M}{(1 + M/2\bar{r}_o)(1 + M/2\bar{r})} \frac{\bar{r}_{<}^l}{\bar{r}_{>}^{l+1}}. \tag{2.22}$$

With the conformally-flat values of a , b , and c , $\Gamma(r_o)$, given by Eq. (2.19), becomes

$$\begin{aligned}
\Gamma(r_o) &= \left[(l+1)F(l+2, l+1/2; 2(l+1); 2M/r_o) F(-l, -l-1/2; -2l; 2M/r_o) \right. \\
&\quad \left. + lF(-l+1, -l-1/2; -2l; 2M/r_o) F(l+1, l+1/2; 2(l+1); 2M/r_o) \right]^{-1} \\
&= \frac{\tilde{E}}{2l+1} \left[F(-l, -l-1/2; -2l; 2M/r_o) F(l+1, l+1/2; 2(l+1); 2M/r_o) \right]^{-1} \\
&= \frac{\tilde{E}}{2l+1}, \tag{2.23}
\end{aligned}$$

where the second equality follows from the second identity of Eq. (15.1.13) of [37] applied to $F(l+2, ; ;)$ and $F(l+1, ; ;)$, and the third equality from the first identity of Eq. (15.1.13) of [37] applied to both hypergeometric functions. Substituting this results into Eq. (2.18) yields

$$C(r_o) = \sqrt{\frac{4\pi}{2l+1}} \frac{\mu}{M}. \tag{2.24}$$

Finally, inserting Eq. (2.22) and Eq. (2.24) into Eq. (2.15) gives

$$K(r) = 2\mu \frac{\sqrt{4\pi/(2l+1)}}{(1 + M/2\bar{r}_o)(1 + M/2\bar{r})} \frac{\bar{r}_{<}^l}{\bar{r}_{>}^{l+1}}, \tag{2.25}$$

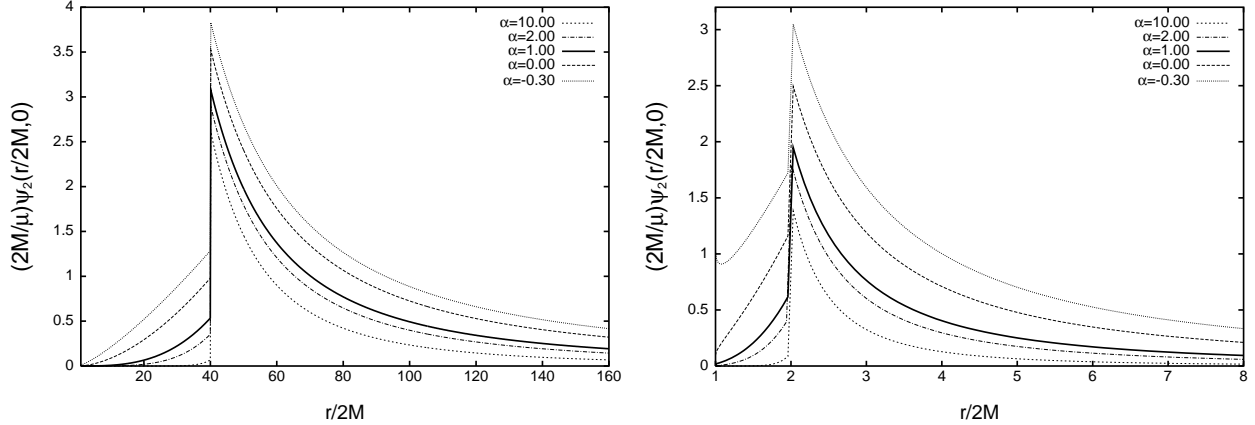


FIG. 1: Initial values of $\psi(r, t)$ for $l = 2$; the particle is initially located at $r_o/2M = 40$ (left) and $r_o/2M = 2$ (right). In both cases $\psi(r, 0)$ is peaked and discontinuous at the particle's location, $r = r_o$. Decreasing (increasing) the value of α increases (decreases) the amplitude and width of the initial pulse. These properties can be associated with the amount of gravitational radiation present on the initial hypersurface. For fixed α , the amplitude of the peak decreases with decreasing r_o .

which is indeed the conformally-flat solution of Eq. (2.11).

In order for the perturbed metric to be real (as opposed to complex), the solutions to Eq. (2.14) must be real functions. Thus, α must be such that the parameters a and b , as listed in Eqs. (2.17), are real. It is easy to verify that the quantity appearing under the square root will be positive if $\alpha \geq \alpha_+$, or $\alpha \leq \alpha_-$, where

$$\alpha_{\pm} = -l(l+1) \pm \sqrt{(l+2)(l+1)l(l-1)}. \quad (2.26)$$

It can be verified that α_+ varies between -1.10102 (when $l = 2$) and -1 (for $l \rightarrow \infty$). On the other hand, α_- monotonically decreases from -10.8990 (when $l = 2$) as l increases. Hence, the metric functions will be real for all values of l if α is restricted by $\alpha \geq -1$.

Figure 1 displays the Zerilli-Moncrief function $\psi(r, 0)$ for the cases $r_o/2M = 40$ and $r_o/2M = 2$. The figure shows that $\psi(r, 0)$ is peaked at the particle's location, and its amplitude and width change with the value of α ; the function is discontinuous at $r = r_o$ because of the discontinuity in the term $\partial K/\partial r$ appearing in Eq. (2.2). We see that the amplitude of the peak increases with decreasing values of α , and this effect is more pronounced as r_o decreases. Intuitively, we associate a smaller (larger) amplitude with a smaller (larger) amount of gravitational radiation initially present in the spacetime. Thus,

to initial data with a small (large) value of α we associate a large (small) amount of initial radiation.

III. NUMERICAL RESULTS

A. Numerical Method

We now describe the numerical method used to integrate Eq. (2.3), starting with the initial data constructed in the preceding section. We recall that the source term is given by Eq. (2.7); special care must be given to the fact that $S(r, t)$ is singular at $r = r_p(t)$, the trajectory of the infalling particle. A numerical method was presented by Lousto and Price [19] and we employ it here with a slight modification, which we discuss below.

The numerical domain is a staggered grid in r^* and t , with a stepsize $\Delta \equiv \Delta r^*/4M = \Delta t/2M$, over the region of spacetime bounded by the spacelike hypersurface $t = 0$ (the moment of time symmetry), a null hypersurface approximating the event horizon [located at $u = T - r_p^*(T)$, where T is given by Eq. (2.8) with $r_p(T)/2M = 1.0001$]⁴, and a null hypersurface approximating future null-infinity [located at $v/2M = (t + r^*)/2M \approx 1500$]. The Zerilli-Moncrief function is extracted from the numerical data on this last hypersurface, i.e. $\psi(r, t)$ is evaluated at $v/2M \approx 1500$ and expressed as a function of $u = t - r^*$. The results presented in Sec. IIIB were obtained by setting $\Delta = 0.01$ in the evolution scheme presented below.

The finite-difference method must take into account the source term, which is non zero (and singular) on the world-line of the infalling particle. The numerical grid is divided into cells of area $4\Delta^2$. (Instead of using the physical area $2\Delta^2$, we found it convenient, following Lousto and Price[19], to use $A = \int dudv = 4\Delta^2$.) The cells can be separated into two groups. The first group corresponds to cells in which $r \neq r_p(t)$ everywhere; these cells are never traversed by the particle. The second group is such that $r = r_p(t)$ somewhere within the cell; these cells are traversed by the infalling particle. The two types of cells are displayed in Fig. 2; in the diagram, the particle enters the cell on the right of r_b^* , and leaves

⁴ This choice is made to ensure that the particle's contribution to the radiation is (almost) zero at the end of the numerical integration. This means that the value of u associated with the event horizon in our numerical grid changes every time we change r_o .

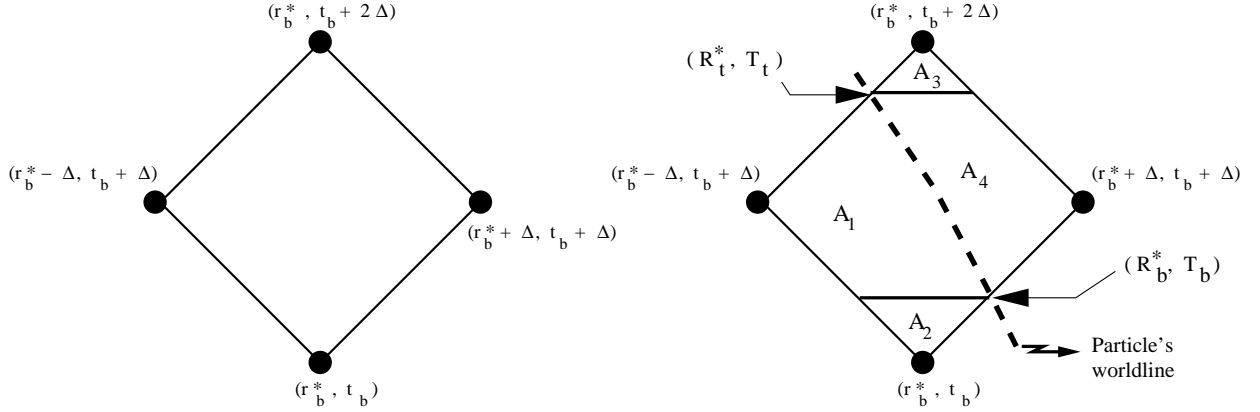


FIG. 2: The left cell is never crossed by the particle's trajectory. In such a cell the evolution of $\psi(r, t)$ is unaffected by the source term in Eq. (2.3), and Eq. (3.1) is used to evolve $\psi(t, r)$ forward in time. The right cell is traversed by the particle's world line. The areas shown in the cell are used in the numerical algorithm that incorporates the effect of the source term in Eq. (2.3). The wave function is evolved according to Eq. (3.5). The labels (R_b^*, T_b) and (R_t^*, T_t) refer to the points (r^*, t) at which the particle enters and leaves the cell, respectively.

on the left.

The evolution of $\psi(r^*, t)$ across cells belonging to the first group is not affected by the source term. For these cells, we use a standard scheme, accurate to $\mathcal{O}(\Delta^4)$, for the homogeneous wave equation in the presence of a potential:

$$\psi(r_b^*, t_b + 2\Delta) = -\psi(r_b^*, t_b) + \left[\psi(r_b^* + \Delta, t_b + \Delta) + \psi(r_b^* - \Delta, t_b + \Delta) \right] \left[1 - \frac{\Delta^2}{2} V_b \right] \quad (3.1)$$

where (r_b^*, t_b) designates the bottom corner of the cell (see Fig. 2), and $V_b = V(r_b^*)$.

The evolution of $\psi(r, t)$ across cells belonging to the second group is affected by the singular source term. To obtain the evolution of ψ across these cells, we closely follow Lousto and Price[19], carefully keeping terms up to order $\mathcal{O}(\Delta^3)$. Integrating Eq. (2.3) over a grid cell, term by term, we get:

$$\int \int dA \left(-\frac{\partial^2}{\partial t^2} + \frac{\partial^2}{\partial r^{*2}} \right) \psi = -4 \left[\psi(r_b^*, t_b + 2\Delta) + \psi(r_b^*, t_b) \right. \\ \left. - \psi(r_b^* - \Delta, t_b + \Delta) - \psi(r_b^* + \Delta, t_b + \Delta) \right], \quad (3.2)$$

$$\int \int dA V(r^*) \psi = V(r_b^*) \left(A_1 \psi(r_b^* - \Delta, t_b + \Delta) + A_2 \psi(r_b^*, t_b) \right. \\ \left. + A_3 \psi(r_b^*, t_b + 2\Delta) + A_4 \psi(r_b^* + \Delta, t_b + \Delta) \right) + \mathcal{O}(\Delta^3), \quad (3.3)$$

where $dA = du dv$, and the A_i 's are areas dividing the cell into four non-equal parts (as shown in Fig. 2). The integration of the source term over the cell eliminates the δ -function in Eq. (2.7) and the term involving the derivative of the δ -function is evaluated by integrating by parts. The result is

$$\begin{aligned} \int \int dA S = & -\kappa \int_{T_b}^{T_t} dt \frac{f(t)}{\Lambda(t)^2} \left[\frac{6M}{r_p(t)} (1 - \tilde{E}^2) + \lambda(\lambda + 1) - \frac{3M^2}{r_p(t)^2} + 4\lambda \frac{M}{r_p(t)} \right] \\ & \pm \kappa \left\{ \frac{f(T_b)}{\Lambda(T_b)} [1 \mp \dot{r}_p^*(T_b)]^{-1} + \frac{f(T_t)}{\Lambda(T_t)} [1 \pm \dot{r}_p^*(T_t)]^{-1} \right\}, \end{aligned} \quad (3.4)$$

where κ is defined by $l(l+1)\tilde{E}\kappa \equiv 16\pi\mu\sqrt{(2l+1)/(4\pi)}$, $\dot{r}_p^* = -\sqrt{\tilde{E}^2 - f/\tilde{E}}$, $f(t) \equiv f(r_p(t))$, $\Lambda(t) \equiv \Lambda(r_p(t))$, T_b is the time at which the particle enters the cell, and T_t the time at which it leaves the cell. In the previous expression, the upper (lower) sign for the first boundary term (a function of T_b) applies when the particle enters the cell on the right (left) of r_b^* . Similarly, the upper (lower) sign for the second boundary term (a function of T_t) applies when the particle leaves the cell on the right (left) of r_b^* .

Substituting the previous results in Eq. (2.3) and solving for $\psi(r_b^*, t_b + 2\Delta)$, we obtain

$$\begin{aligned} \psi(r_b^*, t_b + 2\Delta) = & -\psi(r_b^*, t_b) \left[1 + \frac{V_b}{4}(A_2 - A_3) \right] \\ & + \psi(r_b^* + \Delta, t_b + \Delta) \left[1 - \frac{V_b}{4}(A_1 + A_3) \right] \\ & + \psi(r_b^* - \Delta, t_b + \Delta) \left[1 - \frac{V_b}{4}(A_4 + A_3) \right] \\ & - \frac{1}{4} \left(1 - \frac{V_b}{4}A_3 \right) \int \int dAS(r, t). \end{aligned} \quad (3.5)$$

Notice that we have kept the factor of $(1 - \frac{V_b}{4}A_3)$ in front of the source term. This factor does not appear in the scheme devised by Lousto and Price[19], but is required to obtain quadratic convergence: the boundary terms appearing in Eq. (3.4) are $\mathcal{O}(1)$ in Δ and $\frac{V_b}{4}A_3$ represents a correction of order $\mathcal{O}(\Delta^2)$ to their contribution, which we cannot neglect if we want quadratic convergence.

The previous equations cannot be used to evolve ψ from the initial time $t = 0$ to the next time $t = \Delta$. To get $\psi(r_b^*, \Delta)$ we need $\psi(r_b^* - \Delta, 0)$, $\psi(r_b^* + \Delta, 0)$, and $\psi(r_b^*, -\Delta)$. By construction, $\psi(r_b^*, -\Delta)$ is not known, but we can use the simple relation $\psi(r_b^*, -\Delta) = \psi(r_b^*, \Delta) + \mathcal{O}(\Delta^3)$ which holds by virtue of the fact that the data at $t = 0$ is time-symmetric: $\partial\psi/\partial t = 0$. This relation is valid so long as $r_p^*(t) \neq r_b^*$ everywhere in the cell. We chose $r_b^* - \Delta < r_p^*(0) < r_b^*$ which, for radial infall, guarantees that the relation holds.

The gravitational waveform produced by the infalling particle is given directly by $\psi(u)$, which is extracted from the numerical data in the way described previously. Other quantities of interest are the energy radiated and its power spectrum. We calculate these by first taking a fast Fourier transform of the wave function $\psi(u)$. This is given by

$$\tilde{\psi}(\omega) = \int_{-\infty}^{\infty} d\omega e^{i\omega u} \psi(u), \quad (3.6)$$

where ω is the frequency. From Eq. (2.9) and Parseval's theorem, we find that the power spectrum is

$$\frac{d}{d\omega} E_l = \frac{1}{64\pi^2} \frac{(l+2)!}{(l-2)!} \omega^2 |\tilde{\psi}(\omega)|^2. \quad (3.7)$$

The total energy radiated in each multipole moment is calculated by performing a Romberg integration over all frequencies.

B. Waveforms

The radiation arriving at the null boundary of our domain of integration contains radiation from the initial data, radiation emitted by the particle as it falls toward the black hole, and radiation corresponding to the black-hole's response to the perturbation. Because the particle is at rest at $t = 0$, it initially produces very little radiation. The early part of the waveform is therefore dominated by radiation contained in the initial data. As time proceeds, the radiation produced by the particle becomes noticeable, and the dynamics associated with the perturbation of the event horizon starts to play a role. The radiative process can therefore be separated into three stages. The first stage is associated with the initial data, the second with the infalling particle, and the third with the event-horizon dynamics. We now describe these stages in detail.

The initial data is time-symmetric, and it therefore consists of two radiation pulses: one pulse is outgoing, and the other is incoming. The outgoing pulse proceeds to infinity, with some backscattering [which is small, unless the pulse originates in the strong-field region of the spacetime ($r^* \leq 0$)]. On the other hand, the ingoing pulse moves toward the black hole and is backscattered by the potential barrier at $r^* \approx 0$. The reflected pulse then proceeds to infinity, where it arrives delayed with respect to the original outgoing pulse. This is the first stage of the radiative process, and it is directly associated with the initial data.

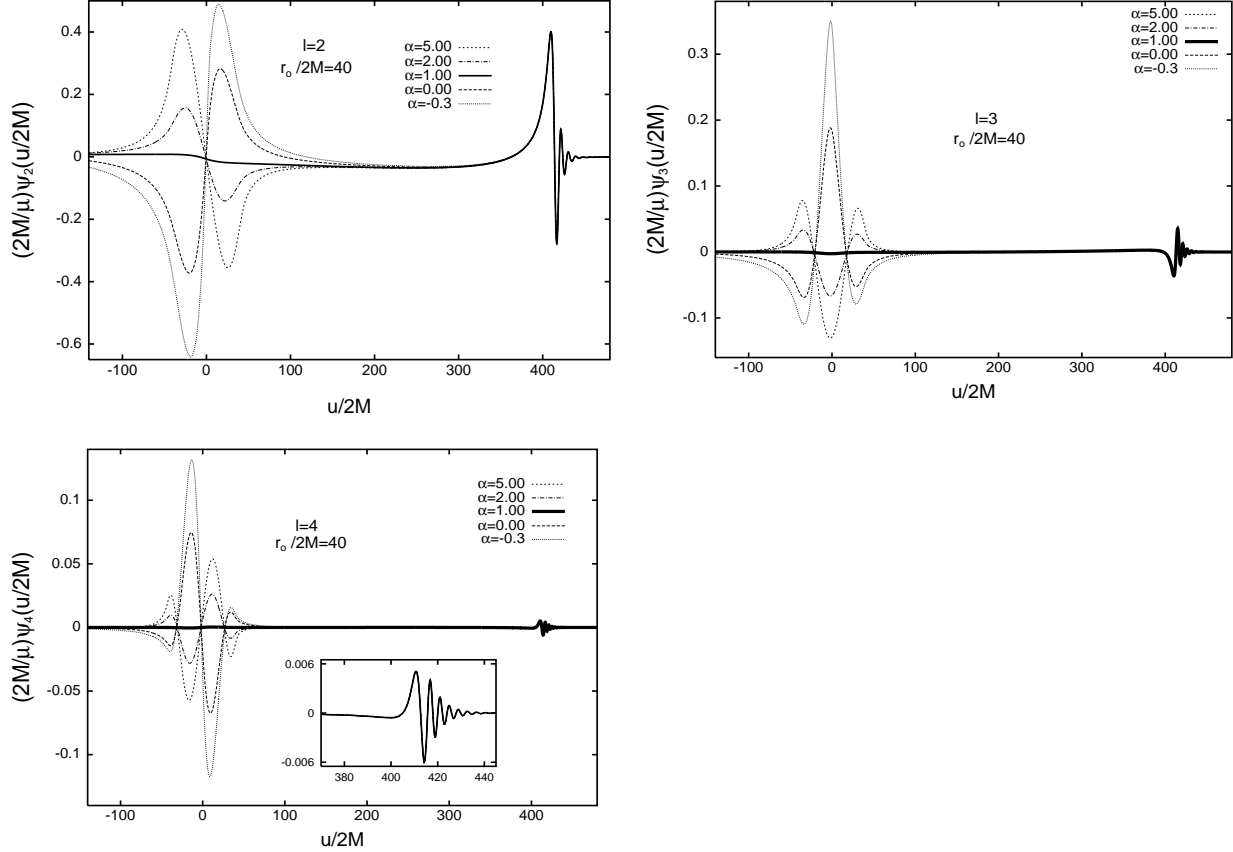


FIG. 3: The $l = 2, 3$, and 4 modes of the Zerilli-Moncrief function for infall from $r_o/2M = 40$, for $\alpha = -0.3, 0, 1, 2$, and 5 . For each multipole moment, the early-time behaviour is dominated by the initial data contribution ($u/2M < 350$), while the late-time behaviour is dominated by radiation emitted by the particle in the strong-field region ($350 < u/2M < 400$) and by quasi-normal ringing of the black hole ($u/2M > 400$). The early-time portion of the waveforms (first stage) depends strongly on the parameter α , which labels the choice of initial data. In contrast, the late-time portion (second and third stages) are completely insensitive to the choice of initial data.

The second stage is associated with the motion of the particle. As the particle accelerates toward the black hole, it produces radiation which propagates to infinity. This happens either by direct propagation or by backscattering from the potential barrier. The third and final stage of the radiative process is the response of the black hole to the perturbation. As the particle approaches the black hole, it tidally deforms the event horizon, which becomes dynamical. The radiation produced in this process interacts strongly with the potential barrier outside the black hole, and the result, after transmission to infinity, is a pattern of

damped oscillations. This response of the black hole to the perturbation created by the particle is known as quasi-normal ringing[38].

As long as $r_o \gg 2M$, the different stages of the radiative process can be clearly distinguished (initial-data pulses, acceleration radiation, and quasi-normal ringing). But when r_o is comparable to $2M$, the three epochs become confused, and this gives rise to interfering waveforms. For this reason, varying the initial separation between the particle and the black hole can have an important effect on the gravitational waveforms.

Let us describe more fully the first stage of the radiative process. For infall from a large distance ($r_o \gg 2M$), the outgoing pulse travels directly to future null-infinity with very little backscattering, since the pulse originates in a region where the potential $V(r)$ is weak. This is shown in the waveform as a single pulse of radiation at early times ($u \approx -r_o^*$). The ingoing pulse, on the other hand, proceeds toward the black hole, where it is almost entirely backscattered by the potential barrier. The reflected pulse then proceeds to infinity and this gives rise to a second pulse of radiation at $u \approx r_o^*$. Varying α changes the amount of gravitational radiation initially present at $t = 0$, and the amplitude of the two pulses depends on α . This can be seen in Fig. 3, where the $l = 2, 3$, and 4 modes of the Zerilli-Moncrief function are displayed for infall from $r_o/2M = 40$, for several values of α . For $l = 2$, the two pulses have a minimum amplitude when $\alpha = 1$, and the amplitudes vary smoothly with α .

At later times, once the pulses have made their way to infinity, the radiative process becomes dominated by the particle's contribution; this is the second stage. At this time, the particle has entered the strong-field region of the spacetime, the acceleration is large, and it radiates strongly. This stage lasts for a short time, because the particle quickly falls into the black hole. The burst of radiation from the particle is then quickly replaced by the third stage, quasi-normal ringing. When $r_o \gg 2M$, the acceleration radiation and the quasi-normal ringing stages are insensitive to the choice of initial data. This is illustrated in Fig. 3.

The situation changes when r_o is chosen within the strong-field region of the spacetime. The outgoing pulse from the initial data still proceeds directly to infinity with little backscattering, creating a pulse at $u \approx -r_o^*$ (see Fig. 4). However, the ingoing pulse is no longer entirely backscattered by the potential barrier; part of the pulse is now transmitted to the black hole. The backscattered portion of the ingoing pulse proceeds to infinity where it generates a second pulse at $u \approx r_o^*$, while the transmitted pulse reaches the event horizon. As a

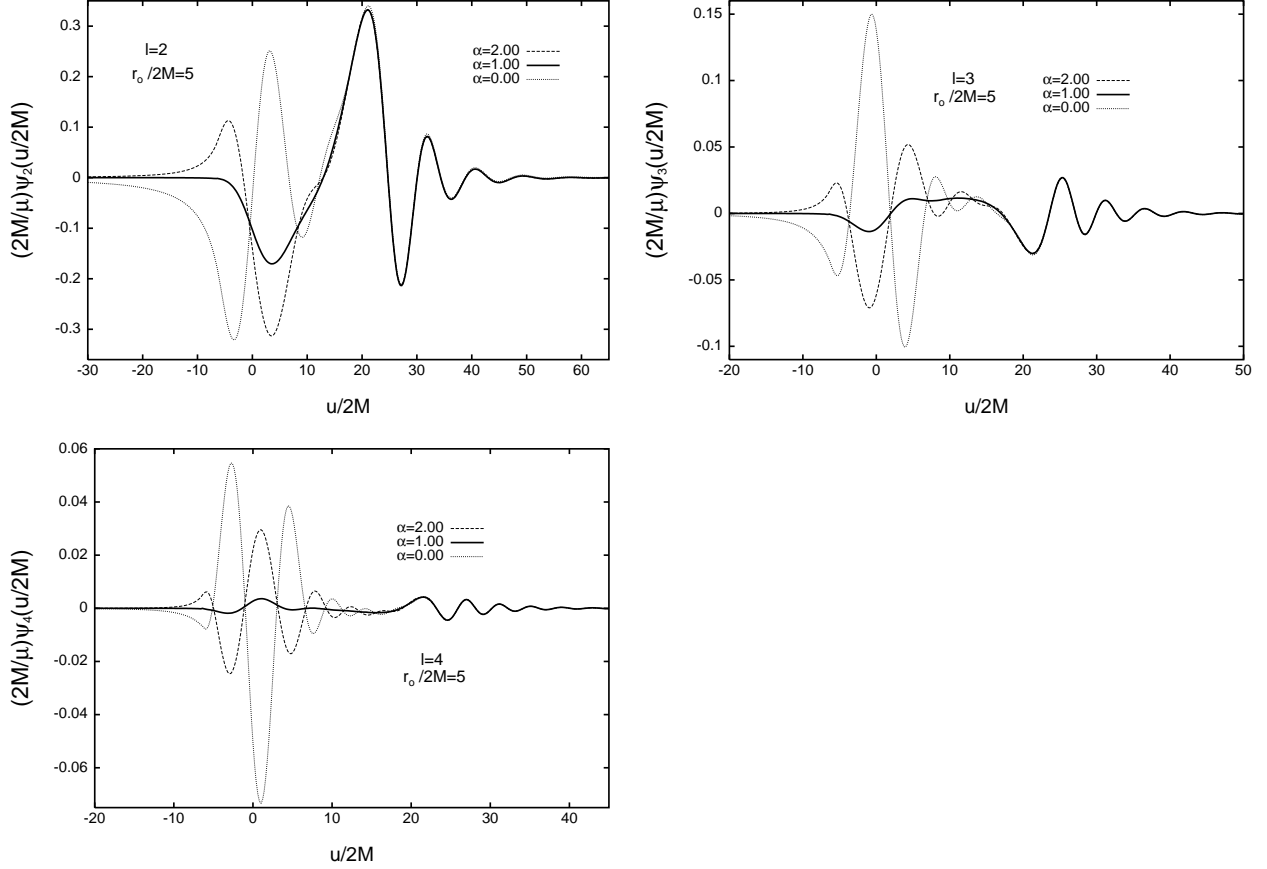


FIG. 4: The $l = 2, 3$, and 4 modes of the Zerilli-Moncrief function for infall from $r_o/2M = 5$, for $\alpha = 0, 1$, and 2 . The waveform changes smoothly as α is varied away from 1 (conformal flatness), but the change is more dramatic when α is decreased. The three stages of the radiative process now overlap and become confused. However, we still witness an early-time sensitivity, and a late-time insensitivity, to the choice of initial data.

result, the event horizon becomes distorted, and starts radiating into quasi-normal modes; the second pulse is therefore immediately followed by an epoch of quasi-normal ringing excited by the transmitted pulse. The amplitude of the quasi-normal ringing depends on the strength of the excitation, and is therefore highly sensitive to the choice of initial data. This early epoch of quasi-normal ringing cannot be seen for infall from large r_o , because in that case the initial data contains mostly low-frequency gravitational radiation that is almost totally reflected by the Zerilli-Moncrief potential[39].

For intermediate values of r_o ($4 \lesssim r_o/2M < 10$), the particle starts in the strong-field region of the spacetime, and its large acceleration causes it to radiate strongly almost im-

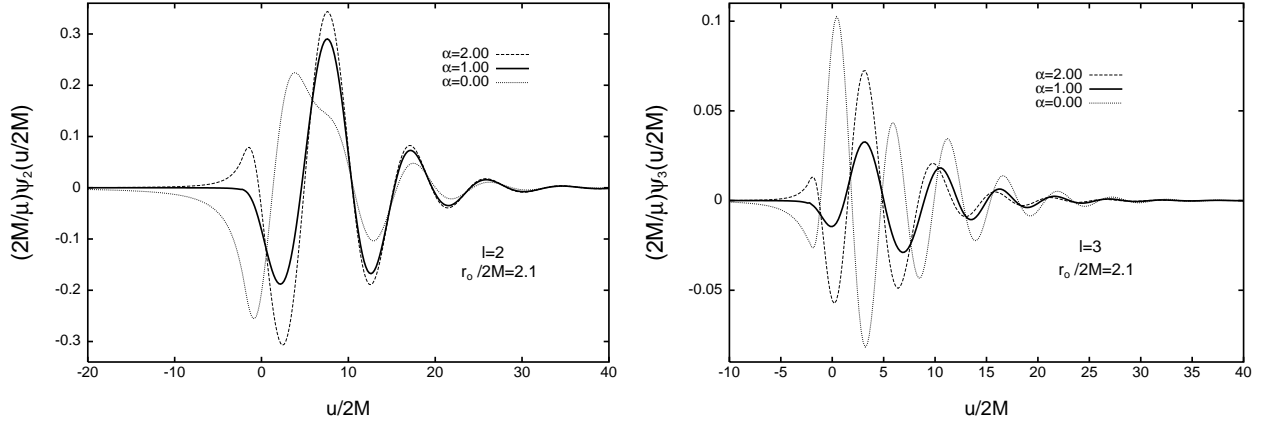


FIG. 5: The $l = 2$ and 3 modes of the Zerilli-Moncrief function for a particle falling from $r_o/2M = 2.1$, for $\alpha = 0, 1$, and 2 . At intermediate times, the waveform is a superposition of the backscattered ingoing pulse from the initial data, and acceleration radiation from the particle. The choice of initial data has an influence at late times; it affects the amplitude and the phase of the quasi-normal ringing.

mediately. The second stage, which for infall from large r_o was dominated by acceleration radiation, is now the sum of acceleration radiation and quasi-normal ringing excited by the initial ingoing pulse, as was discussed above. This can be seen especially clearly for the $l = 3$ and 4 modes of the Zerilli-Moncrief function displayed in Fig. 4, for infall from $r_o/2M = 5$. The superposition can be seen in the interval $5 < u/2M < 20$; it is small for $\alpha = 1$, but large for $\alpha \neq 1$. The third stage of the radiative process is the quasi-normal ringing of the black hole, excited by the particle as it reaches the event horizon. This phase of quasi-normal ringing is to be distinguished from the earlier phase associated with the transmitted pulse; this new phase is insensitive to the choice of initial data.

As r_o is decreased further ($1.3 \lesssim r_o/2M \lesssim 4$), the waveforms become increasingly confused. In this range of initial separations, the particle radiates strongly immediately, and the reflected pulse of ingoing radiation does not reach infinity before the radiation from the particle becomes significant. The interference between these two contributions to the waveform is fairly small, because the particle radiates for a short time before passing through the event horizon. Figure 5 displays the $l = 2$ and 3 modes of the Zerilli-Moncrief function for infall from $r_o/2M = 2.1$ for $\alpha = 0, 1$, and 2 . The interference between the backscattered ingoing pulse and the radiation emitted by the particle is apparent, especially for $l = 2$ and

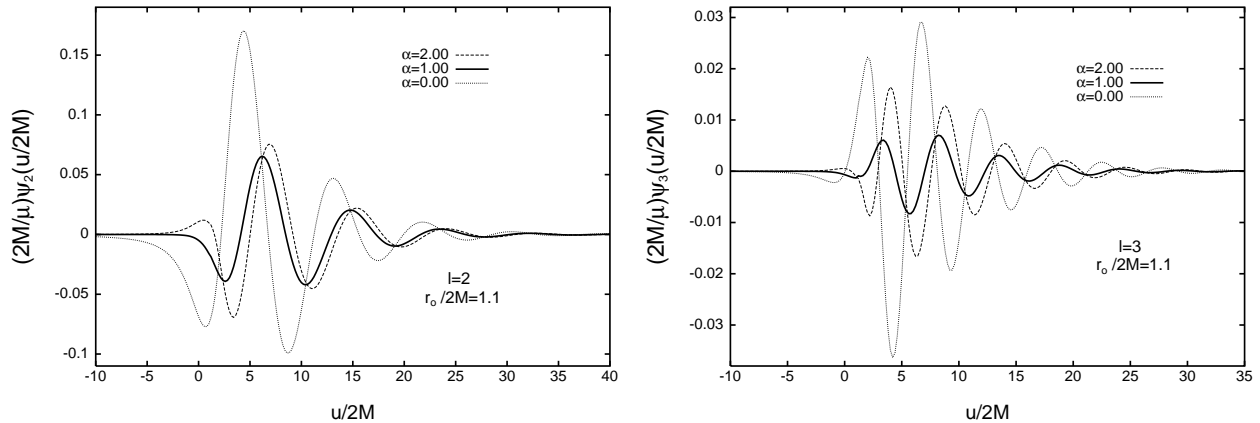


FIG. 6: The $l = 2$ and 3 modes of the Zerilli-Moncrief function for a particle falling from $r_o/2M = 1.1$, for $\alpha = 0, 1$, and 2 . For this very small initial separation, the particle is quickly absorbed by the black hole and cannot radiate much. The initial value of $\psi(r, t)$ determines how strongly the event horizon is distorted, and it therefore has a major impact on the quasi-normal ringing phase of the radiation.

$\alpha = 0$. A new phenomenon is observed for these values of r_o : the stage of pure quasi-normal ringing is now affected by the choice of initial data. The event horizon is distorted both by the transmitted ingoing pulse and the particle, and these factors act at roughly the same time. Different choices of initial data will therefore affect differently the amplitude and the phase of the quasi-normal ringing. This is displayed in Fig. 5.

These effects disappear when r_o is moved past the potential barrier ($1 < r_o/2M \lesssim 1.3$). In such cases, most of the outgoing pulse in the initial data is reflected by the potential barrier, and does not register at infinity. Instead, the pulses in the initial data and the radiation from the particle work together to distort the event horizon. For these very small r_o , the quasi-normal ringing is the only feature that remains in the waveforms. The amplitude and the phase of the quasi-normal ringing are very sensitive to the choice of initial data, because the information about the initial distortion of the event horizon is entirely encoded in the initial data (see Fig. 6 for the case $r_o/2M = 1.1$). The contribution from the particle is minimal because it is almost immediately absorbed by the black hole.

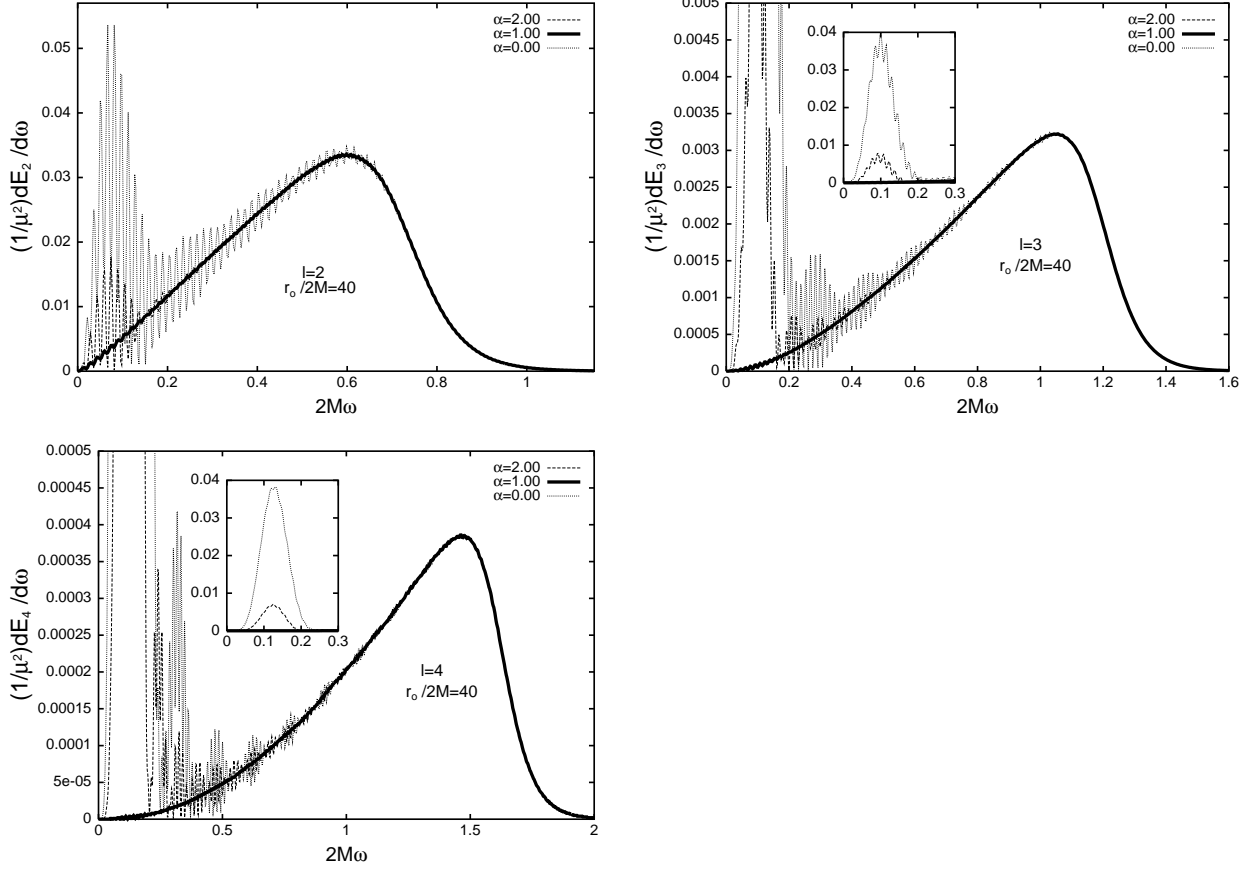


FIG. 7: Power spectra for the $l = 2, 3,$ and 4 modes of the Zerilli-Moncrief function for $r_o/2M = 40$, and $\alpha = 0, 1,$ and 2 . Varying α changes the shape of the spectra at low frequencies, but the effect disappears at high frequencies. The low-frequency oscillations are more important for $\alpha = 0$, compared with $\alpha = 1$ and 2 , and $\alpha = 2$ produces more oscillations than $\alpha = 1$. The low-frequency part of the spectrum is due mostly to the low-frequency gravitational waves contained in the initial data.

C. Power Spectra

The power spectra, as calculated from Eq. (3.7) with a fast Fourier transform algorithm, tell a similar story. For a given choice of l , α , and r_o , the total power spectrum is the sum of initial-data, particle, and quasi-normal ringing contributions, but it includes interference between these contributions.

The interference is important when the pulses associated with the initial data, the acceleration radiation, and the quasi-normal ringing contain overlapping frequencies. Typical

frequencies are $\omega_o \sim r_o^{-1}$ for the initial-data radiation, $\omega_p \sim r_p^{-1}$ for the acceleration radiation, and $\omega_{QN} \sim M^{-1}$ for the quasi-normal ringing. As was mentioned in Sec. III B, the particle emits mostly in the strong-field region of the spacetime ($\omega_p \sim M^{-1}$) and consequently, the interference between acceleration radiation and quasi-normal ringing is always present, while interference with the initial-data contribution is important only when r_o is not much larger than $2M$. In other words, interference effects involving the initial-data pulses are important when the particle is released in the strong-field region. This picture is somewhat simplistic, but it serves as a useful guide to determine when interference effects become important. Our numerical results are consistent with this picture.

For large initial separations ($r_o/2M \gg 1$), we expect the energy spectrum to be the direct sum of the powers in the initial-data and particle contributions, and in the quasi-normal ringing, without much interference. This is confirmed in Fig. 7, where the spectra for the $l = 2, 3$, and 4 modes of the Zerilli-Moncrief function for $r_o/2M = 40$, and $\alpha = 0, 1, 2$, are presented. At low frequencies, the initial data manifests itself as a strong pulse which dominates the spectrum. At higher frequencies, acceleration radiation and quasi-normal ringing dominate the spectrum; this part of the spectrum is easy to recognize, as it does not change when α is varied. As we move away from conformal flatness ($\alpha = 1$), the influence of the initial data spreads into higher frequencies. This can be seen as oscillations in the spectrum (cf. the cases $\alpha = 0$ and 2 in Fig. 7). These oscillations are also present for $\alpha = 1$, but increasing or decreasing the value of α increases their amplitude and the extent by which they spill into higher frequencies. In general, a choice of initial data with $\alpha < 1$, instead of $\alpha \geq 1$, produces larger oscillations, and the effect extends to higher frequencies. (The oscillations are the smallest when $\alpha = 1$.)

We have seen in the previous section that for intermediate values of r_o ($4 \lesssim r_o/2M < 10$), the choice of initial data affects the shape of the waveforms up to times where acceleration radiation starts to dominate the radiative process. For these initial separations, interference effects are important. This is confirmed by our numerical simulations of infall from $r_o/2M = 5$. The spectra, for this value of r_o , are displayed in Fig. 8 for $l = 2, 3$, and 4, and $\alpha = 0, 1$, and 2. For $l = 2$, initial data with $\alpha > 1$ tend to amplify the features apparent for $\alpha = 1$ (see the case $\alpha = 2$ in Fig. 8), while decreasing the value of α changes the location of the maxima; local minima appear in the spectrum where maxima were seen for $\alpha = 1$ (see $\alpha = 0$ in Fig. 8). For $l = 3$ and 4 and $\alpha > 1$ ($\alpha < 1$), we observe a similar amplification

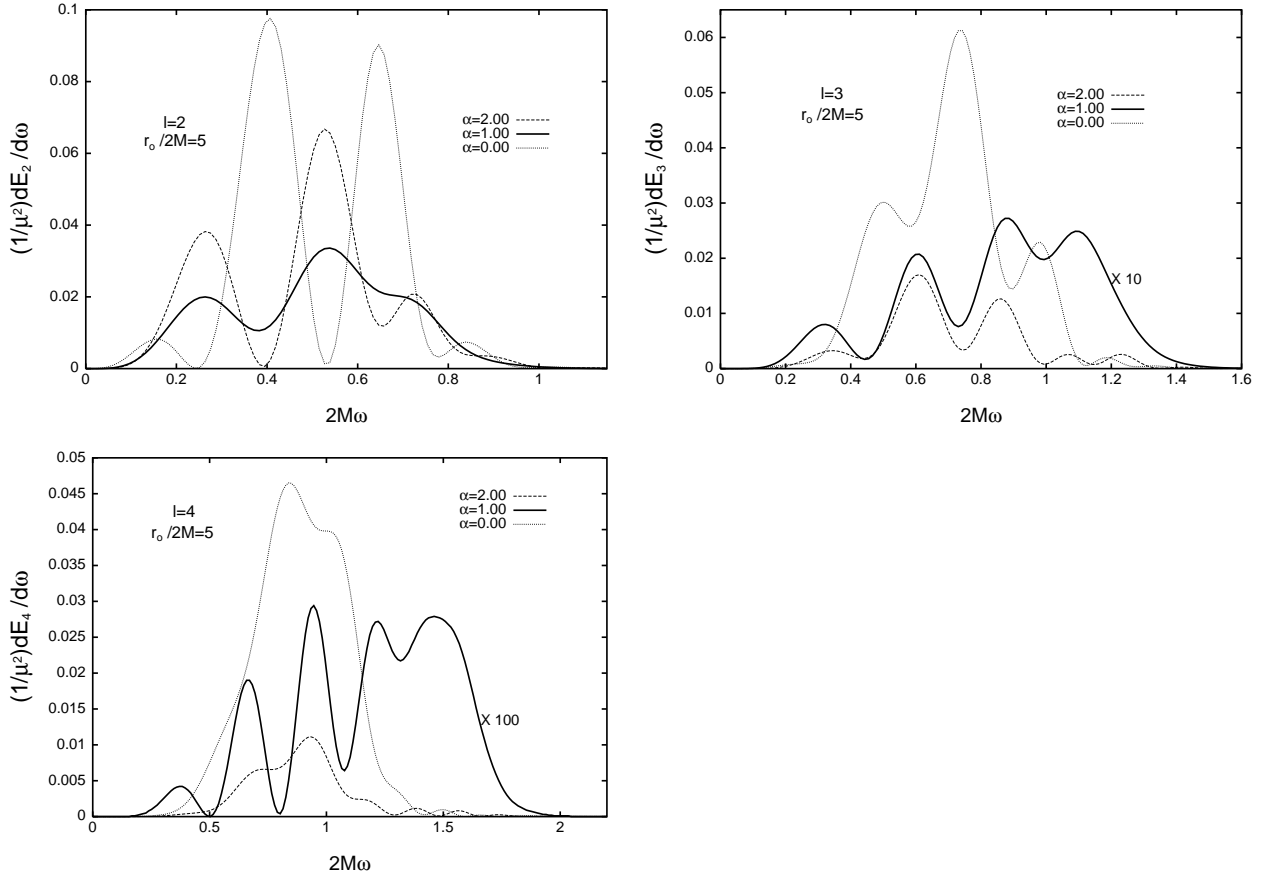


FIG. 8: Power spectra for the $l = 2, 3$, and 4 modes of the Zerilli-Moncrief function for infall from $r_o/2M = 5$, and $\alpha = 0, 1$, and 2 . Interference between the initial-data pulses, the acceleration radiation, and the quasi-normal ringing plays a crucial role in determining the shape of the spectra. For $\alpha = 0$ and $l = 2$, the spectrum has two maxima at $2M\omega = 0.4065$ and $2M\omega = 0.6455$, frequencies at which the spectra for $\alpha = 1$ and 2 have a local minimum. Similarly, the maximum at $2M\omega = 0.5364$ for $\alpha = 1$ and 2 is replaced by a minimum when $\alpha = 0$. This is indicative of strong interference effects. The labels “ $\times 10$ ” and “ $\times 100$ ” indicate the amount by which the amplitude of these two spectra were multiplied to be presented in the same figure.

(attenuation) of the features present for $\alpha = 1$, but the effect is much weaker than for $l = 2$.

As r_o is taken closer to the potential barrier ($1.3 \lesssim r_o/2M \lesssim 4$), the interference becomes less important. In Sec. III B, we showed that for r_o close to the potential barrier, the particle does not radiate strongly before passing through the event horizon, and the interference is small because of the small amount of acceleration radiation. In Fig. 9 we present the spectra for infall from $r_o/2M = 2.1$, $\alpha = 0, 1$, and 2 , and $l = 2$, and 3 . Although interference effects

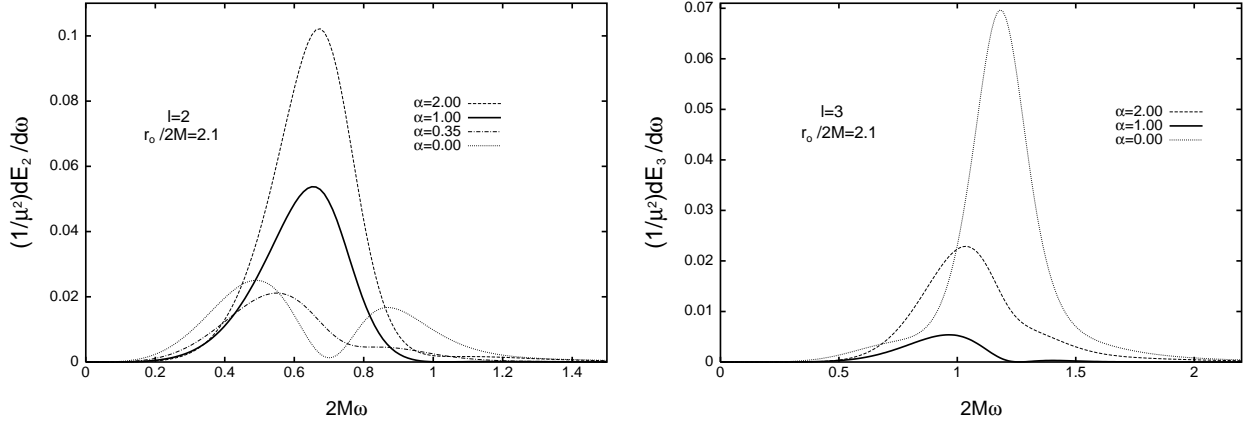


FIG. 9: Power spectra for the $l = 2$ and 3 modes of the Zerilli-Moncrief function for infall from $r_o/2M = 2.1$, and $\alpha = 0, 1$, and 2 . For $l = 2$, we also display $\alpha = 0.35$, to show the smooth transition between the single-maximum and two-maxima regimes described in the text. For such a small separation, acceleration radiation is small, and the interference effects are not very pronounced. They still, however, play an important role in determining the shape of the spectra. The spectrum for $l = 2$ and $\alpha = 0$ has a shape that indicates strong interference effects between initial-data, particle, and quasi-normal ringing contributions: the single maximum at $2M\omega = 0.6553$, seen for $\alpha = 1$ and 2 , is replaced by two maxima at $2M\omega = 0.4915$ and $2M\omega = 0.8697$.

are not as important as for infall from $r_o/2M = 5$, they still play a role in determining the shape of the spectrum, as can be seen for the case $\alpha = 0$. In this case, the spectrum has two maxima and a single minimum; this minimum occurs close to the fundamental quasi-normal frequency, which suggests a strong destructive interference between initial-data-excited and particle-excited quasi-normal ringing. This is different from the cases $\alpha = 1$ and 2 , for which the spectra contain a single peak, indicating that most of the energy is radiated into quasi-normal modes.

Interference effects, such as the ones shown in Fig. 9, have been observed previously by Lousto[40], but in a different context. Instead of evolving the perturbed Misner solution, appropriate for a head-on collision in perturbation theory, Lousto chose to use the full Misner solution[35] as initial data for the Zerilli-Moncrief function. He then evolved these initial data using Eq. (2.3). In this case, the interference is due to the non-linear nature of the initial data he evolved.

Finally, when r_o is chosen well inside the potential barrier ($1 < r_o/2M \lesssim 1.3$), the

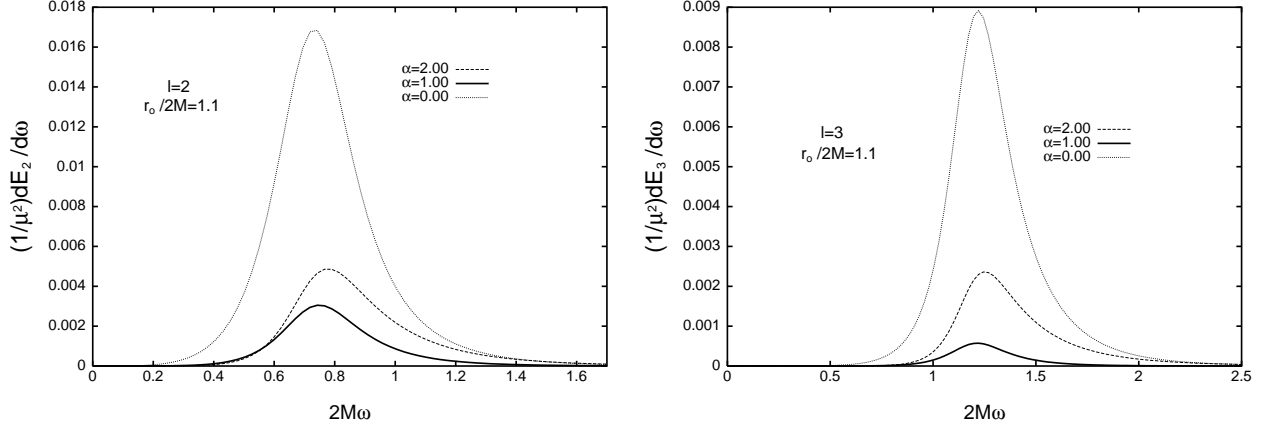


FIG. 10: Power spectra for the $l = 2$ and 3 modes of the Zerilli-Moncrief function for infall from $r_o/2M = 1.1$, and $\alpha = 0, 1$, and 2 . For r_o well inside the potential barrier, acceleration radiation is negligible since the particle is absorbed by the black hole immediately. The initial data distorts the event horizon, which becomes dynamical and starts radiating at its quasi-normal frequencies. The amplitude of the quasi-normal ringing is determined by the strength of the tidal distortion exerted on the event horizon by the initial data. For the cases displayed, the lowest amplitude is obtained for $\alpha = 1$, while the highest is obtained for $\alpha = 0$.

interference effects mentioned previously disappear. For small r_o , the magnitude of the tidal distortion applied to the event horizon is affected only by the choice of initial data. Since the radiation is then dominated by quasi-normal ringing created by the initial tidal distortion of the black hole, the spectra contain a single peak, and its position is independent of α . The choice of initial data affects only the amplitude of the quasi-normal ringing, and this is reflected in the amplitude of the spectra at the fundamental quasi-normal frequency. For infall from $r_o/2M = 1.1$, displayed in Fig. 10 for $l = 2$ and 3 , and $\alpha = 0, 1$, and 2 , the lowest amplitude occurs for $\alpha = 1$, while the highest occurs for $\alpha = 0$.

D. Total Energy Radiated

In this subsection we calculate the total energy radiated as a function of α for infall from $r_o/2M = 40$, and as a function of r_o for six selected values of α . We also tabulate the total energy radiated (the sum of the $l = 2, 3$ and 4 modes) for selected values of r_o and α . The radiated energy was calculated using two different methods: direct numerical integration of

Eq. (2.9), and numerical integration of Eq. (3.7). In this way, the accuracy of the algorithms used could be tested. The results were found to agree to better than 1%. For comparison, we include in our figures the energy radiated by a particle falling from infinity, as calculated by Davis, Ruffini, Press, and Price (DRPP)[41]. The DRPP result for the energy radiated in the $l = 2$ mode is $(2M/\mu^2)E_2 = 1.84 \times 10^{-2}$.

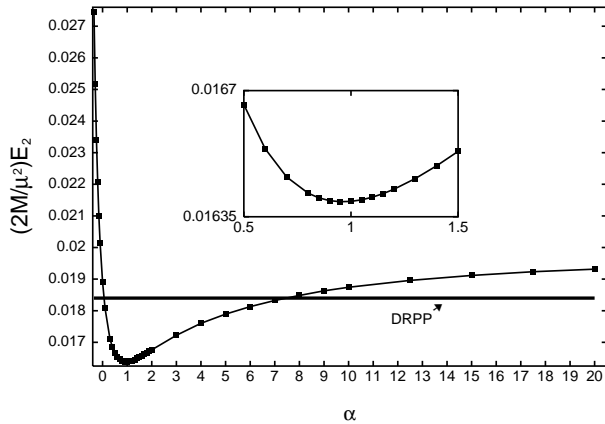


FIG. 11: The total energy radiated in the $l = 2$ mode as a function of α for a particle falling in from $r_o/2M = 40$. Outside of the range $0 < \alpha < 7.5$, the total energy radiated exceeds the DRPP result. The energy is minimized for $\alpha \approx 1$.

We have seen that for large initial separations, the different contributions to the gravitational radiation do not interfere. The energy emitted in each multipole is then the direct sum of the energy contained in the initial-data pulses, the energy emitted in the acceleration radiation, and the energy radiated in the quasi-normal modes. In Sec. III B we showed that all choices of initial data result in two pulses at early times: the outgoing pulse and the backscattered ingoing pulse. These pulses have the smallest amplitude when $\alpha = 1$. Hence, for large initial separations, the waveforms obtained with $\alpha = 1$ are the ones that carry the least amount of energy to infinity.

The total energy radiated in the $l = 2$ mode is shown in Fig. 11 as a function of α , for $r_o/2M = 40$. We see that the energy is minimized for $\alpha \approx 1$, and that it exceeds the DRPP result if α is outside the interval $0 \lesssim \alpha \lesssim 7.5$. For such a large value of the initial radius, we confirm the general belief that the radiated energy is minimized if the initial hypersurface is conformally flat[42, 43].

In Fig. 12 we plot the total energy radiated in the $l = 2$ mode as a function of r_o for

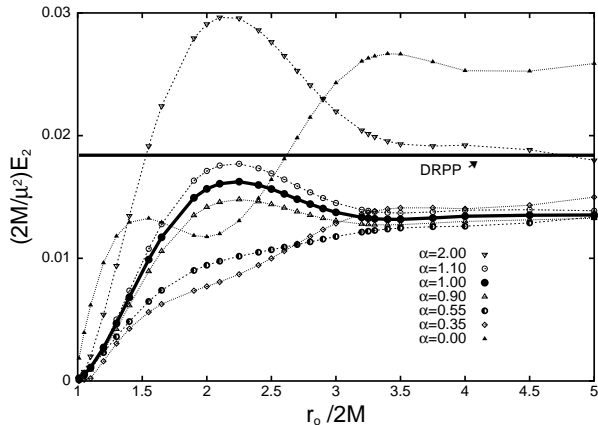


FIG. 12: The total energy radiated by the $l = 2$ mode as a function of r_o . Displayed are six curves corresponding to the values $\alpha = 0, 0.55, 0.9, 1, 1.1,$ and 2 . For these small values of r_o , $\alpha = 1$ no longer minimizes the energy radiated. Instead, the value of α that minimizes the energy changes with r_o . This reflects the interference between the initial data, the particle, and the quasi-normal ringing contributions to the radiation. We were unable to find a single value of α that minimizes the energy in the interval $1 < r_o/2M \leq 5$.

selected values of α . In the range $1 < r_o/2M \leq 5$, the energy is no longer minimized by the choice $\alpha = 1$. Instead, we find that in the interval $2.7 < r_o/2M \leq 5$, the energy is minimized when $\alpha = 0.55$, while in the interval $1 \leq r_o/2M \leq 2.7$, the minimum is achieved when $\alpha = 0.35$. (These values are approximate, as we found it difficult in practice to locate the true minimum in the energy for a given r_o and l .) We also find that for a given r_o , no value of α minimizes the energy radiated for all modes. For example, for infall from $r_o/2M = 5$ there is a minimum in the energy for the $l = 3$ and 4 modes when $\alpha = 0.9$, but this value of α does not minimize the energy in the $l = 2$ mode (see Table I).

Although we are unable to find a single value of α that minimizes the energy radiated for all l and over the whole interval $1 < r_o/2M \leq 5$, we see that in the cases considered, the total energy radiated is never minimized by choosing initial data with $\alpha > 1$. Instead, for infall from a small r_o , it is minimized by a choice of $\alpha < 1$. This is due to strong interference effects for initial data with $\alpha < 1$ when r_o is in the strong-field region of the spacetime; this interference was discussed in Secs. III B and III C.

In Table I we display the total energy radiated in the $l = 2, 3,$ and 4 modes of the

TABLE I: Total energy radiated (in units of $2M/\mu^2$) for the $l = 2, 3$, and 4 modes, and $\alpha = 0.75, 0.8, 0.85, 0.9$, and 1.0 . The sum of the first three multipole moments is denoted by \mathbf{E} . For infall from short and intermediate distances, the minimum in \mathbf{E} is achieved for $\alpha < 1$.

$r_o/2M$	l	$\alpha=0.75$	$\alpha=0.8$	$\alpha=0.85$	$\alpha=0.9$	$\alpha=1.0$
10.0	2	1.467e-2	1.464e-2	1.463e-2	1.464e-2	1.469e-2
	3	1.961e-3	1.876e-3	1.820e-3	1.789e-3	1.790e-3
	4	4.835e-4	3.778e-4	3.045e-4	2.595e-4	2.406e-4
	E	1.711e-2	1.690e-2	1.675e-2	1.669e-2	1.672e-2
5.0	2	1.305e-2	1.309e-2	1.316e-2	1.326e-2	1.353e-2
	3	1.725e-3	1.610e-3	1.546e-3	1.529e-3	1.606e-3
	4	5.600e-4	3.883e-4	2.761e-4	2.156e-4	2.249e-4
	E	1.534e-2	1.509e-2	1.498e-2	1.500e-2	1.536e-2
3.0	2	1.221e-2	1.246e-2	1.274e-2	1.305e-2	1.374e-2
	3	1.359e-3	1.307e-3	1.323e-3	1.398e-3	1.693e-3
	4	5.285e-4	3.298e-4	2.147e-4	1.721e-4	2.681e-4
	E	1.410e-2	1.410e-2	1.428e-2	1.462e-2	1.570e-2
2.1	2	1.238e-2	1.310e-2	1.383e-2	1.457e-2	1.608e-2
	3	1.270e-3	1.325e-3	1.446e-3	1.625e-3	2.120e-3
	4	4.134e-4	2.515e-4	1.757e-4	1.748e-4	3.598e-4
	E	1.406e-2	1.468e-2	1.545e-2	1.637e-2	1.856e-2
1.1	2	9.158e-4	9.068e-4	9.066e-4	9.144e-4	1.099e-3
	3	2.017e-4	1.892e-4	1.854e-4	1.894e-4	2.250e-4
	4	2.286e-4	5.415e-5	4.654e-5	4.529e-5	5.966e-5
	E	1.346e-3	1.150e-3	1.139e-3	1.149e-3	1.384e-3

Zerilli-Moncrief function, for selected values of α and r_o . In general, the features presented previously for the case $l = 2$ are also present for higher multipole moments: the total energy radiated in a given multipole is not minimized by the conformally-flat choice of initial data ($\alpha = 1$), but by some $\alpha < 1$. We find that in some cases, the interference effects become so

important that the energy radiated increases with the multipole order l , e.g. $E_2 < E_3 < E_4$. This increase in energy with increasing l contradicts our slow-motion expectation, according to which the energy radiated should decrease with increasing multipole order. A typical example of this phenomenon is displayed in Table I for $r_o/2M = 1.1$ and $\alpha = 0.75$: here we find $E_4 > E_3$.

IV. CONCLUSION

A one-parameter family of time-symmetric initial data for radial infall of a particle into a Schwarzschild black hole was introduced in perturbation theory. The family is parameterized by α , which measures the gravitational-wave content of the initial surface. The family contains a conformally-flat initial three-geometry as a special member ($\alpha = 1$). Varying α allowed us to examine the influence of the initial data on the gravitational waves emitted by the particle-black hole system.

We showed that for large initial separations, three stages can be clearly identified in the radiative process: initial-data-produced pulses, particle-produced acceleration radiation, and black-hole-produced quasi-normal ringing. For smaller separations, the three stages become confused and interference takes place.

For large initial separations we confirmed the general belief that a conformally-flat initial three-geometry minimizes the radiated energy. But we showed that for $r_o/2M < 10$, the initial configuration that minimizes the energy is not the conformally-flat choice. Instead, the configuration that minimizes the gravitational-wave content has $\alpha < 1$.

Most importantly, our numerical simulations show to what extent the gravitational waveforms are influenced by the choice of initial data. As long as the particle falls toward the black hole from a distance $r_o/2M > 10$, the part of the waveform that is associated with acceleration radiation and quasi-normal ringing is insensitive to the choice of initial data. In these cases, waveforms obtained with conformally-flat initial data are an accurate representation of the true radiative process in the region of interest, because the unphysical radiation coming from the initial data propagates to null-infinity before the physical radiation becomes important. For $r_o/2M \lesssim 10$, however, the two contributions interfere, and uncertainties associated with the choice of initial data hopelessly contaminate the waveforms.

Acknowledgement

The authors gratefully acknowledge Thomas Baumgarte for useful correspondence on numerical convergence. This work was supported by the Natural Sciences and Engineering Research Council of Canada.

APPENDIX: CONVERGENCE OF THE NUMERICAL CODE

We now describe the convergence properties of our numerical algorithm. The method described in Sec. III A is designed to be second-order convergent, i.e. the numerical solution converges towards the exact solution quadratically. This means that for a given choice of r_o , α , and l , the field at a fixed spacetime point is a function of Δ described by

$$\psi_N(\Delta) = \psi_A + \Delta^2 \rho, \quad (\text{A.1})$$

where ψ_N is the numerical field obtained with a stepsize Δ throughout the grid, ψ_A is the exact solution, and ρ is an error term independent of Δ . Note that error terms of order $\mathcal{O}(\Delta^3)$ are neglected in this equation.

The convergence of our numerical code can be tested by defining

$$\delta\psi(\Delta) = \psi_N(2\Delta) - \psi_N(\Delta) = 3\Delta^2 \rho, \quad (\text{A.2})$$

and evaluating $\delta\psi$ for various values of Δ . This function is proportional to the error made in discretizing Eq. (2.3) and it satisfies $\delta\psi(n\Delta) = n^2\delta\psi(\Delta)$. This latter property is important as we use it to determine the convergence rate of our code. We construct $\delta\psi$ from ψ calculated with $\Delta = 0.005, 0.01, 0.02$, and 0.04 on the null line $v/2M = 500$, i.e. at each grid point on this ingoing null line we calculate $\delta\psi(0.005)$, $\delta\psi(0.01)$, and $\delta\psi(0.02)$. In this way, we construct $\delta\psi(\Delta)$ as a function of retarded time u . Note that for $u < -r_o^*$, we are testing the vacuum finite-difference algorithm, whereas for $u > -r_o^*$ we are testing the convergence properties of the code involving the cells crossed by the particle's world line.

From the definition of $\delta\psi$, it is obvious that they should satisfy $\delta\psi(0.02) = 4\delta\psi(0.01) = 16\delta\psi(0.005)$ at every grid point if Eq. (A.1) holds and the convergence is quadratic. In Fig. 13, we display $\delta\psi(0.02)$, $4\delta\psi(0.01)$, and $16\delta\psi(0.005)$, for the case $r_o/2M = 2.1$, $\alpha = 1$, and $l = 2$. The fact that the three curves are close together signals quadratic convergence, with $4\delta\psi(0.01)$ and $16\delta\psi(0.005)$ being the closest. This is expected since as Δ is decreased,

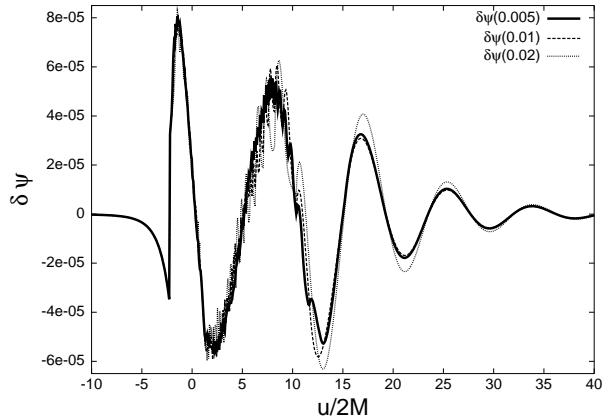


FIG. 13: Convergence properties of our numerical code. We display $\delta\psi(0.02)$, $4\delta\psi(0.01)$, and $16\delta\psi(0.005)$, for $r_o/2M = 2.1$, $\alpha = 1$, and $l = 2$. The agreement between the curves indicates that the numerical code is converging quadratically towards the exact solution. This is characteristic of the convergence in other cases.

the approximation made in Eq. (A.1) becomes more accurate, and we get a better coincidence between the curves. The convergence rate observed in this figure is typical of the convergence obtained for other choices of r_o , α , and l .

By varying the location of the event horizon, and the location of future-null infinity, we have verified that our results are independent of the actual location of the null boundaries. We also verified that our results for $\alpha = 1$ are consistent with the results presented by Lousto and Price[28].

-
- [1] S.F. Portegies Zwart, S.L.W. McMillan, *Ap. J. Lett.* **528**, L17 (2000).
 - [2] G.B. Cook *et al.*, *Phys. Rev. Lett.* **80**, 2512 (1998).
 - [3] R. Gómez *et al.*, *Phys. Rev. Lett.* **80**, 3915 (1998).
 - [4] P. Anninos, D. Hobill, E. Seidel, L. Smarr, W.-M. Suen, *Phys. Rev. Lett.* **71**, 2851 (1993);
P. Anninos, D. Hobill, E. Seidel, L. Smarr, W.-M. Suen, *Phys. Rev. D* **52**, 2044 (1995).
 - [5] M. Alcubierre, B. Brüggmann, D. Pollney, E. Seidel, R. Takahashi, *gr-qc/0104020* (2001).
 - [6] A.M. Abrahams *et al.*, *Phys. Rev. Lett.* **80**, 1812 (1998).
 - [7] P. Anninos, S. Brandt, P. Walker, *Phys. Rev. D* **57**, 6158 (1998).
 - [8] S. Brandt *et al.*, *Phys. Rev. Lett.* **85**, 5496 (2000).

- [9] K.C.B. New, D.-I. Choi, J.M. Centrella, P. MacNeice, M.F. Huq, K. Olson, Phys. Rev. D **62**, 084039 (2000).
- [10] J. Baker, M. Campanelli, C.O. Lousto, gr-qc/0104063 (2001).
- [11] L. Lehner, (submitted to Class. Quant. Grav.), gr-qc/0106072 (2001).
- [12] M. Miller, (submitted to Phys. Rev. D), gr-qc/0008017 (2000).
- [13] J. Thornburg, Class. Quant. Grav. **4**, 1119 (1987).
- [14] G.B. Cook *et al.*, Phys. Rev. D **47**, 1471 (1993).
- [15] S. Brandt, B. Brügmann, Phys. Rev. Lett. **78**, 3606 (1997).
- [16] J. Bowen, Gen. Relativ. Gravit. **11**, 227 (1979); J.M. Bowen, J.W. York, Phys. Rev. D **21**, 2047 (1980).
- [17] G.B. Cook, Living Rev. Rel. **3**, 5 (2000).
- [18] A. Garat, R.H. Price, Phys. Rev. D **61**, 124011 (2000).
- [19] C.O. Lousto, R.H. Price, Phys. Rev. D **56**, 6439 (1997).
- [20] C.O. Lousto, R.H. Price, Phys. Rev. D **57**, 1073 (1998).
- [21] P. Anninos, R.H. Price, J. Pullin, E. Seidel, W.-M. Suen, Phys. Rev. D **52**, 4462 (1995).
- [22] G. Khanna *et al.*, Phys. Rev. Lett. **83**, 3581 (1999).
- [23] K. Alvi, Phys. Rev. D **61**, 124013 (2000).
- [24] J. Pullin, Prog. Theor. Phys. Suppl. **136**, 107 (1999).
- [25] J. Baker, B. Brügmann, M. Campanelli, C.O. Lousto, Class. Quant. Grav. **17**, L149 (2000).
- [26] A.M. Abrahams, R.H. Price, Phys. Rev. D **53**, 1963 (1996).
- [27] R.H. Price, J. Pullin, Phys. Rev. Lett. **72**, 3297 (1994).
- [28] C.O. Lousto, R.H. Price, Phys. Rev. D **55**, 2124 (1997).
- [29] C.W. Misner, K.S. Thorne, and J.A. Wheeler, *Gravitation* (Freeman, San Francisco, 1973).
- [30] F.J. Zerilli, Phys. Rev. D **2**, 2141 (1970).
- [31] T. Regge, J.A. Wheeler, Phys. Rev. **108**, 1063 (1957).
- [32] V. Moncrief, Annals of Physics **88**, 323 (1974).
- [33] C.T. Cunningham, R.H. Price, V. Moncrief, Ap. J. **230**, 870 (1979).
- [34] J.N. Goldberg, A.J. MacFarlane, E.T. Newman, F. Rohrlich, and E.C.G. Sudarshan, J. Math. Phys. **8**, 2155 (1967).
- [35] C.W. Misner, Phys. Rev. **118**, 1110 (1960); C.W. Misner, Ann. Phys. **24**, 102 (1963).
- [36] R.W. Lindquist, J. Math. Phys. **4**, 938 (1963); D.R. Brill, R.W. Lindquist, Phys. Rev. **131**,

- 471 (1963).
- [37] M. Abramowitz, I.A. Stegun, *Handbook of Mathematical Functions with Formulas, Graphs, and Mathematical Tables* (U.S. Govt. Print. Off., Washington, 1964).
 - [38] E.W. Leaver, Proc. R. Soc. London **A402**, 285 (1985).
 - [39] S. Chandrasekhar, *The Mathematical Theory of Black Holes* (Oxford University Press, New York, 1983).
 - [40] C.O. Lousto, Phys. Rev. D **63**, 047504 (2001).
 - [41] M. Davis, R. Ruffini, W.H. Press, R.H. Price, Phys. Rev. Lett. **27**, 1466 (1971).
 - [42] J.W. York, Jr., Phys. Rev. Lett. **26**, 1656 (1971).
 - [43] M.D. Duez, T.W. Baumgarte, S.L. Shapiro, Phys. Rev. D **63**, 084030 (2001).